

A Case Study of Contrail Evolution Over The Great Lakes

David P. Duda

Hampton University, Hampton, VA 23668

Patrick Minnis, Louis Nguyen

Atmospheric Sciences, NASA Langley Research Center, Hampton, VA 23681

Rabindra Palikonda

AS&M, Inc., Hampton, VA 23681

(Article submitted to the Journal of the Atmospheric Sciences)

David P. Duda, NASA Langley Research Center, MS 420, Hampton, VA 23681-2199. email:
d.p.duda@larc.nasa.gov.

Abstract. Widespread persistent contrails over the western Great Lakes during 9 October 2000 were examined by using commercial flight data, coincident meteorological data, and satellite remote sensing data from several platforms. The data were used together to determine the atmospheric conditions under which the contrails formed and to measure several contrail physical properties, including the areal coverage, the spreading rate, the fall speed and the optical properties of the contrails. Most of the contrails were located between 10.6 and 11.8 km in atmospheric conditions consistent with a modified form of the Appleman contrail formation theory. However, the RUC-2 model analyses have a dry bias in the upper tropospheric relative humidity with respect to ice (RHI), as contrail generation during the outbreak was simulated best by using $\text{RHI} > 85\%$ as a threshold. In regions with negative vertical velocities over 0.015 m s^{-1} , no contrails formed even when the RHI was above the threshold. Areal coverage by linear contrails peaked at $30,000 \text{ km}^2$, but the maximum contrail-generated cirrus coverage was over twice as large. Contrail spreading rates averaged around 2.7 km hr^{-1} , and the contrails were visible in the 4-km GOES imagery approximately 1 hour after formation. Contrail fall speed estimates were between 0.00 and 0.045 m s^{-1} based on observed contrail advection rates. Optical depth measurements ranged from 0.1 to 0.7 , with consistent differences between remote sensing methods. Contrail formation density was roughly correlated with air traffic density after the effects of competing cloud coverage, humidity and vertical velocity were considered. Improved tropospheric humidity measurements are needed for realistic simulations of contrail and cirrus development.

1. Introduction

Contrails are a source of anthropogenic cloudiness. Similar in physical properties to natural cirrus, contrails affect the atmospheric radiation budget and may influence climate. Because air traffic is expected to grow by 2 to 5% annually for the next 50 years, contrail coverage will also increase and may produce a significant amount of radiative forcing by 2050 (Minnis et al., 1999). Unfortunately, current estimates of global contrail radiative forcing are extremely uncertain, and range over almost two orders of magnitude (Minnis et al., 1999; Meyer et al., 2002) as a result of large discrepancies in global estimates of contrail coverage and optical properties, and the co-occurrence of contrails over other clouds. Current theoretical estimates of global contrail coverage (Sausen et al. 1998; Ponater et al. 2002) were tuned to early estimates of linear contrail coverage estimated visually from infrared satellite imagery. The estimates differ based on the parameterization used to diagnose contrails and the numerical weather analyses employed to determine the ambient conditions. Better understanding and more accurate prediction of contrail climatic effects require better estimates of contrail coverage, optical properties and radiative forcing and their relationships to the atmospheric state.

Of particular interest are predictions of widespread outbreaks of persistent contrails in otherwise clear skies, as these contrails are likely to have the largest impact on the global radiative energy budget. Determining the frequency of occurrence and the magnitude of such outbreaks would help refine estimates of global contrail radiative forcing. Additionally, development of reliable methods for diagnosing persistent contrails and their physical and radiative properties from numerical weather analyses is essential for predicting future contrail climate impacts. Toward these goals, this paper studies widespread persistent contrails over the western Great Lakes during 9 October 2000 by using actual flight data, coincident

meteorological data and satellite remote sensing to determine under which conditions this outbreak occurred, to measure the spreading of the contrail amount over time, to observe the evolution of contrail properties during the outbreak, and to test empirical humidity thresholds required for contrail formation and persistence. The results of the analyses should be valuable for improving the parameterization of contrails in climate models.

2. Data

Satellite imagery, flight track data and meteorological data from numerical weather prediction model analyses were used to match individual contrails with flight tracks, and to determine the meteorological conditions under which the contrails formed. A brief description of each dataset is provided below.

2.1 Satellite Data

A large outbreak of persistent contrails developed over the upper peninsula of Michigan and the surrounding region on 9 October 2000. Many of the contrails were visible in the eighth Geostationary Operational Environmental Satellite (*GOES-8*) imager 4-km channel-4 ($10.7\ \mu\text{m}$) infrared brightness temperature ($T_{10.7}$) images and in the channel-4 minus channel-5 ($12.0\ \mu\text{m}$) split-window ($T_{12.0}$) brightness temperature difference (BTD) imagery for at least 3 to 4 hours before dissipating. Data from the *NOAA-14* AVHRR 1-km imager taken at 2050 UTC were also used (see Fig. 1), as well as multispectral 1-km data from the MODerate Resolution Imaging Spectroradiometer (MODIS) on the *Terra* satellite.

Fig. 1

Contrails were identified manually as bright linear features in half-hourly *GOES-8* BTD images from 1015 UTC to 2245 UTC 9 October 2000 (data from 1715 UTC were missing). The contrails were divided into linear segments, and their coordinates were plotted into a database.

2.2 Air Traffic Data

Commercial air traffic data from the FlyteTrax product (FT; FlyteComm, Inc., San Jose, CA) were used to determine flight tracks over the Great Lakes area on 9 October 2000. The database consists of 2-minute readings of aircraft position (latitude, longitude, altitude) for every non-military flight (identified by flight number) over the USA and Canada. A series of these readings for a particular aircraft flight is referred to here as a flight track, and each reading is called a flight track point. Although the FT database does not include military flights, it contains most of the air traffic over the Great Lakes region. All flight track points above 7.6 km (25,000 ft), between 36.5°N and 51°N and between 95°W and 79°W, and for the times between 1000 UTC and 2200 UTC were included in the analysis.

2.3 Meteorological Data

Atmospheric profiles of height, temperature, humidity, and horizontal and vertical wind speeds were derived from the 40-km resolution, 1-hourly Rapid Update Cycle-2 (RUC) analyses (Benjamin et al., 1998) in 25 hPa intervals from 450 hPa (approximately 6.4 km over the Great Lakes) to 175 hPa (12.7 km). The RUC data were linearly interpolated at each pressure level to a 1°×1° grid at 15-minute intervals from 1000 UTC to 2300 UTC 9 October 2000. To minimize the processing time, only a portion of the RUC horizontal domain centered over the Great Lakes (from 36°N to 54°N and from 97°W to 75°W) was used.

3. FLIGHT TRACK ANALYSIS

The satellite, flight track and meteorological data were used together to determine the altitude of contrail formation and the temperature and humidity conditions under which the contrails formed. As a first step in this process, the flight track data were advected to the times

of the satellite observations by using the RUC model winds. The advected flight tracks were then compared with the satellite observations of contrails to determine which aircraft produced contrails. From the RUC meteorological data and contrail position data, the atmospheric conditions in the contrail formation regions could be determined.

3.1 Advection of Flight Tracks

The RUC horizontal winds were used to advect the aircraft flight tracks for each 15-minute interval throughout the period of available data (1000–2200 UTC, hereafter called the analysis period). To simplify the advection scheme, the flight track altitudes indicated in the FT database were converted to pressure levels by using a domain-mean pressure/height profile that was computed hourly from the RUC data. The model winds were interpolated to these levels and used to advect the flight tracks for each time interval. After adjusting the model winds to true north-south (u) and east-west (v) wind speed vectors, the wind speed and bearing of the winds were computed for each 15-minute time step, and great circle navigation formulae were used to compute the new latitude and longitude at each time step.

The flight tracks were also advected vertically using the RUC computed vertical velocities and assumed values for contrail fall speeds. The RUC vertical velocities were converted from units of hPa s^{-1} to m s^{-1} using the hydrostatic approximation. Several fall speed values ranging from -0.03 m s^{-1} to 0.15 m s^{-1} were tested.

3.2 Matching flight tracks with contrails

The flight tracks were matched using a contrail-centered coordinate system assuming a spherical earth. The great circle arc through each linear contrail segment serves as the “equator” of the coordinate system. The “prime meridian” of the each contrail was the great circle placed

perpendicular to the first great circle and centered on the westernmost end of the contrail segment. The longitudinal range of the cloud therefore represented the length of the contrail.

With this coordinate system, the proximity of each flight track to a contrail could be evaluated. For each time step, the shortest distance (D_s) of each flight track point (including current flights and flights advected from an earlier time) from the first great circle was computed using a series of geometric vector operations. If the flight track did not extend across the entire longitudinal range of the contrail, the flight track was not considered. For all other flight tracks, the mean D_s was computed for each flight track segment across the longitudinal range of the contrail. The flight track with the minimum average D_s for all applicable time steps throughout the simulation was chosen as the flight track matching the contrail.

Table 1 shows the flights matched to 11 of the contrails during the analysis period. These Table 1 contrails were arbitrarily chosen, but are expected to be representative of the entire contrail population. To reduce the possibility of mismatches, most of the contrails selected for Table 1 were relatively isolated from nearby contrails. For most of the flights, the selected flight track was obvious as the mean D_s of the selected track was usually less than 12 km and much less than the values from other flights. Note that the selected flight track usually was the best match for all times and when different fall speeds were used, even in cases like ACA163 where other flight tracks had comparable (but larger) values of D_s . For two of the flights, ACA113 and AAL55, our confidence of a match is less due to the large average value of D_s during the analysis period. For all of the selected flights, the altitude of the aircraft ranges between 10.6 km (35,000 ft) and 11.8 km (39,000 ft, roughly between 240 hPa and 200 hPa), and usually 1 hour is necessary for the contrail to become wide enough to become visible in the *GOES-8* 4-km imagery. The typical

width for a contrail was 8 km approximately 2 hours after it was first seen in the *GOES-8* imagery.

4. RETRIEVED CONTRAIL PROPERTIES

The areal coverage of the contrails was determined both subjectively by manual inspection of the BTD imagery and objectively by the automated method of Mannstein et al. (1999). The RUC wind analyses were used to estimate the rate of contrail spreading seen in the satellite imagery, and the fall speeds of the contrails. Multiple satellite remote sensing retrievals of contrail height, optical thickness, particle size and other properties were made for selected groups of evolving contrails. The numerical weather model analyses were also used to determine the conditions necessary for contrail formation. Finally, the FT database was used to relate air traffic density to the observed contrail formation density.

4.1 Areal coverage of contrails

The contrails formed nearly continuously over the western Great Lakes area throughout the analysis period. Once formed, the contrails moved to the southwest into Wisconsin, Indiana, and Illinois where they massed into nearly continuous decks of cirrus clouds before dissipating by 0200 10 October 2000. Automated, objective estimates of linear contrail coverage were made from the *GOES-8* data in an area covering Wisconsin, southern Ontario, the upper peninsula of Michigan, and Lakes Michigan and Superior using the image processing methodology of Mannstein et al. (1999). The areas of analysis were determined by manual inspection of the *GOES-8* imagery and circumscribed by analysis boxes. As the contrails advected, the analysis boxes were moved (and expanded) to track not only new linear contrails, but also the older contrails until they dissipated or could no longer be recognized as originating from contrails. An

Fig. 2

example of the analysis regions is shown in Fig. 2. A subjective analysis of the same regions was also performed by manually inspecting the $T_{10.7}$ minus $T_{12.0}$ images. The contrail coverage in each analysis box was based on the fraction of pixels in which both the magnitude of the mean BTD and the standard deviation in BTD of the 3×3 pixel grid centered on the pixel were larger than arbitrary thresholds. Although the manual inspection was subjective, it allowed for the tracking of contrails that become too diffuse and non-linear to be identified in the automated method.

The Mannstein et al. (1999) algorithm was designed to work with 1-km AVHRR data, while the imagery from *GOES-8* has a nominal resolution of 4 km. The viewing zenith angle in this case is around 53° resulting in a pixel size close to 7 km over the area of interest. In addition, the *GOES-8* $T_{10.7}$ and $T_{12.0}$ images sometimes have across-track line errors that can produce noticeable striping. The objective algorithm can occasionally misclassify this artifact as a contrail (Meyer et al., 2002). To alleviate this problem, a weighted 5-pixel average was used to smooth the differences between scan lines. For each pixel in each scan line, half of the weight is assigned to the line being smoothed, while a total of 40% is divided between the corresponding pixels in the two adjacent lines. The remaining 10% is divided between the corresponding pixels two scan lines away.

Figure 3 shows the time series of contrail coverage determined from both the objective technique and the manual inspection. The plot also shows the areal coverage determined by the objective algorithm at 2050 UTC from the 1-km AVHRR data. The close correspondence between the *GOES*- and AVHRR-derived coverage suggests that, at least in this example, the Mannstein et al. (1999) algorithm may be applicable to 4-km *GOES-8* data. The areal coverages determined from the objective and subjective analyses match each other well between 1015 and

Fig. 3

1645 UTC, but the coverage from the subjective method quickly becomes more than twice that retrieved from the objective algorithm after 1745 UTC, when many of the contrails in the analysis region became too diffuse and too closely clustered together for the algorithm to resolve. At 1745 UTC, the spreading linear contrails covered an area of nearly 25,000 km² over Wisconsin, southern Ontario, the upper peninsula of Michigan, and Lakes Michigan and Superior. By 2045 UTC, the linear contrails that could still be identified as such covered nearly 30,000 km². This coverage does not include the cirrus clouds in northern Illinois and Wisconsin that were formed from older contrails, which more than double the contrail coverage. After 2045 UTC, both the linear contrail coverage and the coverage by contrail-generated cirrus slowly decrease at the end of the analysis period.

4.2 *Contrail spreading*

The increases in contrail areal coverage presented in the previous section are not only caused by increases in the number of contrails, but also by the spreading of individual contrails. Jensen et al. (1998) note that the vertical shear of the horizontal wind is the dominant process driving contrail spreading. From modeling studies they show that both particle sedimentation and the vertical motions within the contrail resulting from longwave radiative heating allow wind shear to spread the contrail. Several factors affect the magnitude and depth of the vertical motions in the contrail, including atmospheric stability, the magnitude of the radiative heating, the contrail ice water path and the cloud microphysics. Jensen et al. (1998) simulate only one case of contrail growth; the relationship between the contrail spreading rates and these factors is not completely known. The conditions for contrail spreading in this study were less favorable than in the Jensen et al. (1998) study since the magnitude of the wind shear between 225 and 250 hPa (where most of the aircraft flights were located) usually ranged between 2 and 4 m s⁻¹ km⁻¹,

compared to $6 \text{ m s}^{-1} \text{ km}^{-1}$ in Jensen et al. (1998). The actual shear affecting the contrails was even less since the direction of the vertical shear was usually not perpendicular to the flight path/contrail direction. Based on the predominant contrail direction (NW to SE), the mean vertical shear of the horizontal wind over the upper peninsula of MI and eastern Lake Superior (hereafter called upMI/eLS) during the analysis period was only $1.5 \text{ m s}^{-1} \text{ km}^{-1}$, while it was $2.8 \text{ m s}^{-1} \text{ km}^{-1}$ over eastern WI (hereafter called eWI). In addition, the atmosphere was slightly more stable in this study. The lapse rate between 225 and 250 hPa was between 7.6 and 8.5 K km^{-1} throughout the analysis period over both upMI/eLS and eWI.

Estimates of contrail spreading from *GOES-8* observations are difficult due to the coarse resolution of the imagery. Observation of groups of trails in the 4-km *GOES-8* imagery suggests that for flight times between 1400-1900 UTC, the trails are about 6 km wide 2.25 hours after flight time, and about 10 km wide 3.75 hours after flight time. An analysis of the RUC wind field over the western Great Lakes shows that the trails formed in a region of light shear ($1 - 3 \text{ m s}^{-1} \text{ km}^{-1}$) that extends to a depth of one or two kilometers below contrail depth, depending on the time of formation. Figure 4 shows the spreading of a contrail based on the RUC wind analyses. The spreading was computed from the wind field by comparing the advection of the contrails assuming a zero sedimentation/vertical deepening rate and the advection of the contrail that is falling/deepening by a specified constant rate. Figure 4 shows that once the contrail particles reach the level of higher shear a couple kilometers below the cloud, they are quickly pulled apart. Thus, only contrails with small, slowly falling particles would remain intact. Figure 4 also shows the contrail spreading rates estimated from the satellite observations. The observed contrail spreading rates are most consistent with contrails deepening at a rate around 0.060 to 0.125 m s^{-1} .

Fig. 4

4.3 Remote sensing analyses

Several remote sensing analyses were performed on the evolving contrails using GOES, MODIS, and AVHRR imagery. From the AVHRR data, an optical depth retrieval was performed using a fixed cloud temperature (FCT) approach similar to that of Meyer et al. (2002). First, the effective emissivity (ϵ) of each contrail pixel (identified by the objective algorithm) was computed from the observed $T_{10.7}$, the observed background temperature T_b , and the contrail temperature T_c using

$$\epsilon = [B(T_{10.7}) - B(T_b)] / [B(T_c) - B(T_b)], \quad (1)$$

where B is the Planck function at 10.7 μm . For this study, T_c was assumed to be 215 K based on the regional mean temperature at 225 hPa. T_b is calculated as the average temperature of all pixels at a distance of 3 pixels horizontally, vertically or diagonally from a contrail pixel that are not adjacent to any other contrail pixel. In addition, T_b must be greater than T_c to ensure that the background pixels measure points below the contrail. If no pixels meeting these criteria are found, the mean background temperature calculated for all other contrail pixels within the local 10' grid box is used. The visible optical depth (τ) of the contrail pixels is then computed from the effective emissivity by inverting the parameterization of Minnis et al (1993),

$$\epsilon = 1 - \exp[a(\tau / \mu)^b], \quad (2)$$

which accounts for the infrared scattering. In (2), μ is the cosine of the viewing zenith angle, and the coefficients $a = -0.458$ and $b = 1.033$, are for an axi-symmetrical 20- μm hexagonal ice column. The average visible optical depth of the linear contrails in the 2050 UTC AVHRR image is 0.14 based on the FCT approach.

The longwave radiative forcing of the contrails was computed directly from the observed radiances. The unit contrail longwave forcing is given as

$$F = (Q_b - Q_c), \quad (3)$$

where Q_c and Q_b are the longwave fluxes for the contrails and background, respectively. The broadband fluxes were determined from the narrowband radiances observed by the satellite using the method of Minnis et al. (1991). The mean longwave forcing of the linear contrails in the AVHRR image (Fig. 1) was 10.4 W m^{-2} .

The retrieval was also performed on two series of *GOES-8* images. The first (Loop A) followed several contrails over the upper peninsula of Michigan and the surrounding area between 1745–1915 UTC, while the second (Loop B) tracked developing contrails over the eastern end of Lake Superior that drifted over the upper peninsula of Michigan and Lake Michigan from 1845 UTC until 2045 UTC. In both cases, most of the contrails in the analysis boxes had appeared in the *GOES-8* imagery 1 hour before the start of the time series. The results of the retrievals are shown in Fig. 5a. The mean retrieved optical depths in Loop A increase from 0.10 at 1745 UTC to 0.17 at 1845 UTC, while the contrails in Loop B start at 0.16 and increase to 0.31 one hour later before decreasing to 0.20 at 2045 UTC. In both time series the contrails reach their maximum in optical depth about 2 hours after appearing in the satellite imagery, or 3 hours after their initial formation. In this analysis, the contrail longwave radiative forcing is nearly exactly proportional to the cloud optical depth (Fig. 5b), and varies from 7.8 to 13.1 W m^{-2} in Loop A and from 12.2 to 21.5 W m^{-2} in Loop B.

Fig. 5

The visible-infrared-solar infrared split-window technique (VISST; Minnis et al. 1995a) was also used to infer the physical properties of the evolving contrails from the *GOES-8* and MODIS data. The VISST simultaneously determines effective particle size, visible optical depth (τ_v), cloud temperature (T_c), and effective cloud height (z_c) from the radiances observed from several GOES channels. Minnis et al. (1995a) describe the algorithm in detail. Using clear-sky

radiance estimates for each channel and the sun/satellite geometry, the VISST computes the spectral radiances expected for both liquid-droplet and ice-water clouds for a range of particle sizes and optical depths. The effective diameters (D_e) for the hexagonal ice column model clouds vary from 6 to 135 μm . The effective cloud height is the altitude or pressure from the nearest vertical temperature profile that corresponds to T_c . The model cloud radiances are computed using the cloud emittance and reflectance parameterizations of Minnis et al. (1998) and a visible channel surface-atmosphere-cloud reflectance parameterization (Arduini et al., 2002). The VISST determines the cloud properties by matching the observed visible (0.65 μm), solar infrared (3.7 μm), and infrared (10.7 μm) radiances to the same quantities computed with the parameterizations and corrected to the top of the atmosphere. The process is iterative and can compute results for both ice and liquid water clouds. In the retrievals presented here, the model assumed all contrail clouds were ice.

VISST retrievals of ice-cloud properties using GOES and other multi-spectral satellite data have been compared to both in situ aircraft measurements (Young et al. 1998; Duda et al. 2002) and passive and active radiometric measurements at surface sites (Mace et al. 1998; Dong et al. 2002). The VISST retrievals show good agreement with the measurements for cloud height and cloud particle size. The derived heights for optically thin cirrus clouds are generally located somewhere between the bottom and center of the cloud (X. Dong, personal communication; Minnis et al. 2002b).

Figure 5a includes the optical depths retrieved by VISST for Loops A and B. Also shown in Fig. 5a is a VISST analysis using *Terra* MODIS data from the 1801 UTC overpass. The VISST optical depths are larger than the corresponding retrievals using the Meyer-based method.

Another section of the contrail outbreak was analyzed from 1645 UTC to 2145 UTC with the VISST retrieval. During this period, several contrails starting over the upper peninsula of Michigan at 1645 UTC spread into a diffuse cloud mass over Wisconsin that could not be identified as linear contrails by the automated algorithm. The white box over Wisconsin in Fig. 2 shows the location of the contrail-generated cirrus at 1945 UTC. Two soundings were used to initialize the retrievals throughout the period (see Fig. 6a). The 0000 UTC sounding from Gaylord, MI (APX) was taken in a region of mid-level cloudiness. The cloudiness appears in the APX sounding as a moist layer (RH as high as 80%) from 2.6 km to 4.8 km. The GRB sounding at 0000 UTC also shows two drier layers (RH near 50%) between 4.2 and 5.1 km and between 5.8 and 7.0 km, but no mid-level cloudiness is apparent at GRB between 1645 and 2145 UTC.

Fig. 6

Figure 7a shows a time series of VISST-retrieved ice crystal sizes for the analyzed scene. Except for the large particle diameters (60 μm) measured at 1645 UTC, the mean particle diameters remain around 27 μm throughout the period. These particle sizes are somewhat smaller than those reported by Duda et al. (2001) for contrails near Hawaii. The smaller sizes are likely the result of competition for atmospheric moisture between the numerous contrails. The large particle sizes retrieved at 1645 UTC may be caused by differences between the back-scattering properties of the actual contrail particles compared to the properties used in VISST. The scattering angle for the observations at 1645 UTC was about 179° . Another source of uncertainty in D_e is the occurrence of some low-level cloudiness in the box at that time.

Fig. 7

Figure 7b presents the τ , retrieved by VISST. After starting near 0.30 at 1645 UTC, the retrieved τ slowly increases over time until a large increase in optical depth occurs between 1845 and 1915 UTC. After 1945 UTC, the retrieved τ decreases quickly, reaching 0.2 by 2145 UTC. Such large changes in optical depth are unexpected in aging contrail cirrus, and it is likely

that these changes are artifacts of the retrieval methods as discussed below. Retrievals of contrail/cirrus properties from visible wavelengths are complicated by the thinness and possible broken nature of the cloud fields, and the heterogeneity of both the clouds and the clear-sky radiances (Minnis et al., 1990). Small errors in calibration or in the retrieval models can produce significant errors in retrieved optical depth, especially when the solar zenith angles are large and the surface properties are highly variable. The derived particle sizes are less sensitive to the optical depth for $\tau_v < 0.5$ because of the small variation in the 3.9-11 μm brightness temperature difference for a given particle size over a range of cloud temperatures and, hence, cloud optical depth. VISST retrievals using the *Terra* MODIS data at 1623 UTC and 1801 UTC are also included in Fig. 7b, and are nearly identical to the results from *GOES-8*.

The variations in retrieved cloud optical depth are also reflected in the retrieval of cloud height shown in Fig. 7c. Since the VISST uses the retrieved τ_v to estimate cloud temperature from the infrared temperature, the small optical depths retrieved at 1645 UTC and after 2015 UTC result in higher effective cloud height at these times. The increase in the derived optical depths between 1915 and 2015 UTC results in an apparent decrease in effective cloud height of nearly 2 km. The VISST rejected some pixels due to cloud shadowing effects, resulting in the retrieval of warmer cloud temperatures, and thus somewhat lower cloud heights. The maximum heights from the VISST retrievals are 2-3 km higher than the mean values, but show similar trends during the day.

Contrail/cirrus heights were derived independently from stereography using combinations of *GOES-8* with MODIS, AVHRR, and simultaneous *GOES-10* (at 135°W) imagery following the method of Fujita (1982). The stereographic results within the VISST analysis region are also shown in Fig. 7c. Since the heights had to be determined from easily recognizable, bright

features in the imagery, the stereographic estimates correspond to the highest portions of the contrail cirrus, and thus are expected to be higher than the VISST results. They are generally within one kilometer of the maximum VISST heights from *GOES-8*. The stereographic height estimate was verified in one contrail by using a concurrent estimate from cloud shadows; both methods derived a height of 10.7 km. The heights of freshly formed contrails (1 to 1.5 hours after formation) ranged from 10.7 to 10.85 km.

4.4 *Contrail formation conditions*

From the classical Appleman (1953) criteria for persistent contrail formation, persistent contrails form when the atmospheric temperature reaches a critical value, and the relative humidity with respect to ice (RHI) is 100% or greater. Widespread cirrus formation is expected to occur above the humidity level required for homogeneous nucleation. Such cirrus would obscure and deplete much of the moisture needed for contrail formation. Sassen and Dodd (1989) developed a theoretical model of the RHI threshold for homogeneous nucleation at temperatures below 238 K. Their results were fit with a polynomial to yield the following RHI threshold for the formation of cirrus,

$$RHI_{cirrus} = 1.09559 \times 10^{-4} T^3 - 7.77598 \times 10^{-2} T^2 + 1.77725 \times 10^1 T - 1160.77 \quad (4)$$

In equation (4), temperature T is in Kelvins, and the nucleation humidity threshold RHI_{cirrus} is in percent. At the mean flight level of the matched flight tracks, RHI_{cirrus} would be 154%. Thus, we would expect the contrail outbreak area to occur within the RHI range from 100 to 154%. Using the method of Schrader (1997) and an appropriate engine efficiency factor for commercial aircraft (Busen and Schumann, 1995), the regions of persistent contrail formation at 225 hPa were computed using the RUC model data. The contrail coverage exceeded the area predicted by classical theory.

The RUC model, like all numerical prediction models, computes a grid-averaged value of relative humidity that can be less than the RHI at individual locations within the grid. Thus, persistent contrails can exist even when the true grid RHI is less than 100%. In addition, upper tropospheric humidity measurements (from radiosondes and other platforms) used in the RUC model analyses often underestimate RHI (Elliot and Gaffen, 1991; Miloshevich et al., 2001), and a dry bias in the model is likely. A comparison of upper tropospheric dew point temperatures between radiosondes and the RUC model on 12 September 2001 shows that the RUC model's moisture scheme may offset some of this bias (Minnis et al. 2002a). While the mean RUC minus radiosonde dew point temperature difference was near 0 K at 400 hPa, the difference increased to around 1.8 K at 250 hPa and to 3.7 K at 150 hPa. These differences in dew point temperature would increase RHI in the northern Great Lakes region by about 20% compared to radiosonde measurements at 225 hPa.

To determine an empirical humidity threshold where persistent contrails are possible, the locations of the persistent contrails identified from the *GOES-8* imagery were compared to the RUC analyses of RHI. Figure 8 shows the paths of all flight tracks at 1745 UTC that occur in the area where the RHI was estimated to be 85% or greater. Nearly all of the contrails fall within this threshold. The largest RHI found in the area where the contrails appear in Fig. 8 was 105%. Fig. 1 shows that cirrus and other clouds covered the remaining portion of the high RHI area south and east of the contrails, where RHI reached as high as 110%. Fig. 8

Minnis et al. (2002a) developed an empirical correction for radiosonde-based RHI measurements based on the observations from Sassen (1997) for temperatures less than 243 K:

$$\Delta RHI(\text{in } \%) = \Delta 1.87 \Delta T(\text{in K}) + 443 \quad (5)$$

$$RHI_{corr} = RHI + \Delta RHI \quad (6)$$

Since the temperature at the mean pressure level of the matched flight tracks was 215 K, the corrected RHI threshold for the contrails in this case would be 126%. The largest corrected RHI in the region containing contrails would be 146%. This corrected RHI range falls within the limits imposed by classical contrail formation conditions and the Sassen-Dodd criteria for homogeneous nucleation of cirrus, even when the expected differences between the RUC and radiosonde values of RHI (20%) are included in the correction. Figure 6b shows the RHI profile for the APX and GRB soundings adjusted by eqs. (5) and (6) for temperatures below 243 K. The APX sounding has adjusted RHIs over 100% between 11.0 and 12.7 km, while the GRB sounding has ice supersaturation between 11.5 and 12.6 km. The height of the supersaturated layer in the soundings is slightly higher than the corresponding RUC analyses, and is likely due to the effect of cold temperatures on the rawinsonde sensor time constant (Miloshevitch et al., 2001).

4.5 *Contrail fall speeds*

Figure 9 shows the matched flight tracks and contrail segments identified from the *GOES-8* imagery at 1745 UTC. Although several of the contrails are well matched to individual flights, the origins of some trails are indeterminate. They may be due to the presence of military flights and limitations in the flight advection/matching scheme. Good matches between the flight tracks and all of the contrails are also unlikely due to uncertainties and errors arising from several sources. These include the initial flight track positions, the estimation of contrail location from the 4-km *GOES-8* imagery, and the advection of the flight tracks using the RUC model winds. The advection of the flight tracks is probably subject to the most uncertainty since the simulated tracks remained at nearly the same pressure level throughout the analysis period (the RUC vertical velocities were small), but the contrails are actually falling continually and are

Fig. 9

influenced by winds at different levels. The mean altitude (pressure level) of the flight tracks that most closely matched the contrails was 10.9 km (36,000 ft, 225 hPa), a value that corresponds closely to the results of the stereographic analysis results in Fig. 7c.

The effects of particle sedimentation on the advection of the contrails were investigated by adjusting the fall speed of the contrails by a constant value. The speeds ranged from -0.03 m s^{-1} to 0.15 m s^{-1} . Estimates of ice crystal fall speeds for maximum dimensions matching the retrieved particle sizes (from 22 to 60 μm) range from about 0.01 to 0.06 m s^{-1} (Pruppacher and Klett, 1980; Heymsfield and Iaquinta, 1999).

As mentioned earlier, the selected flight tracks for the eleven flights shown in Table 1 usually were the best matches for all times, even when different fall speeds were used. For some flights, the mean D_s dropped noticeably when a fall speed was included. Figure 10 shows the mean D_s computed for the flight tracks as a function of the contrail fall speed. The lowest values usually occur when the fall speed is from 0.0 to 0.045 m s^{-1} . For most flights, the D_s values become larger when the fall speed exceeds 0.06 m s^{-1} . Fig. 10 also shows the mean D_s computed for all 11 flights as a function of contrail fall speed (squares). The smallest errors occur when the fall speeds are between 0.015 – 0.03 m s^{-1} . This result suggests that the fall speeds of most of the contrail particles are consistent with the particle sizes retrieved from the VISST.

Fig. 1

The RHI fields from the RUC analyses confirm the conclusion that the contrail fall speeds must be small. The mean RHI at all levels from 200 hPa to 325 hPa remain steady over upMI/eLS until around 1700 UTC, then decrease by 25 to 35% over the next 5 hours. The mean RHI over the region usually remains above the 85% level throughout the analysis period at both 200 and 225 hPa, while at 250 and 275 hPa the mean RHI remains above 85% until approximately 1800 UTC. At lower levels the mean RHI over upMI/eLS is usually less than

85% throughout the analysis period. Over eWI, the changes in RHI over the analysis period are much smaller, usually by less than 10%. The mean RHI is above the 85% threshold at both 200 and 225 hPa throughout most of the analysis period, near the threshold at 250 hPa, and below the threshold at lower levels. Thus, the RUC humidity analyses suggest that the contrail particles would remain in ice-saturated air as long as they did not fall below approximately 260 hPa (10.1 km, or 33,100 ft). Since most flight tracks are around 11 km, and many contrails appear to persist at least 4 hours, the maximum *net* contrail fall speeds based on the RUC RHI analyses would be 0.06 m s^{-1} . Although the results from Fig. 4 suggest a contrail-deepening rate as high as 0.125 m s^{-1} , the net contrail fall speeds may be less since vertical motions in the contrail would loft many of the cloud particles to higher altitudes. In the Jensen et al. (1998) study, the simulated contrail top appears to rise at a rate around 0.10 m s^{-1} , which would be consistent with both the contrail fall speeds presented in Fig. 10 and the contrail deepening rates in Fig. 4.

The fall speed of an individual contrail was measured by using stereography and flight track data. Flight CDN902 was one of the flights identified from the *GOES-8* imagery in Table 1. Estimates of the contrail height from both stereography and cloud shadows were 10.7 km at 1945 UTC. The flight track data shows that the flight passed over the region about 60 min earlier. Since the flight track altitude of CDN902 was 37,000 ft (11.28 km), the estimated contrail fall speed is 0.16 m s^{-1} . This fall rate is slightly higher than the rate derived from contrail advection and spreading.

4.6 *Contrail density versus air traffic density*

To correlate contrail formation with air traffic data, the *GOES-8* imagery was manually inspected over a twelve-hour period (1000 UTC to 2200 UTC) to determine when and where contrails initially formed. Since most contrails appeared in the images approximately 1 hour

after their probable flight track of origin, the contrails were advected backward in time by the mean wind at 225 hPa to estimate their initial location. A time step of 30–50 min back in time produced the best agreement between air traffic and contrail density. The contrail densities within $1^\circ \times 1^\circ$ degree grid boxes from 42°N to 50°N and 92°W and 80°W were computed for each hour, and averaged over the twelve-hour period. Similarly, the air traffic density over the same period and domain was computed. To improve the match between the air traffic and contrail density data, several contrail formation and visibility factors must be considered to determine those regions where contrails would not form or be seen. First, the *GOES-8* imagery was inspected to find where and when non-contrail overcast existed that would obscure contrail detection. Second, those areas with 225 hPa RHI that are below the 85% threshold were selected to account for contrail formation conditions (the temperatures throughout the region were cold enough to satisfy the modified Appleman criteria). An inspection of the satellite imagery and the RUC vertical velocity field at 225 hPa showed that no contrails formed in regions where the RUC vertical velocity was less than -0.015 m s^{-1} , even when the RHI was above the 85% threshold. Thus, all regions where the vertical velocity was less than -0.015 m s^{-1} (sufficiently strong negative motion) were found, and all regions meeting these cloudiness, humidity or vertical velocity criteria were excluded from the air traffic and contrail density calculations. Figure 11 shows a plot of the mean contrail density versus air traffic density for the areas of the grid not affected by the formation and visibility factors. The contrails were advected backward in time by 30 min in the figure. The contrail density appears to be roughly correlated with air traffic density, even though the contrails from only 1 in 10 flights became widespread enough to be detected in the 4-km *GOES-8* imagery.

Fig. 11

5. DISCUSSION

Several physical properties were retrieved from an outbreak of contrails over the western Great Lakes on 9 October 2000 by using a combination of satellite, meteorological and air traffic data sets. Contrail-generated cirrus more than doubled the areal coverage compared to linear contrail coverage estimates derived using the objective analysis. The rate of contrail spreading observed from the *GOES-8* imagery was 2.7 km hr^{-1} . This rate was about half the rate reported in the simulation by Jensen et al. (1998), but their study has larger wind shear and slightly less stable conditions. The estimates of spreading based on the RUC wind analyses suggest that the contrails deepened at a rate around 0.060 to 0.125 m s^{-1} , while the net fall speed of the contrails were less than 0.045 m s^{-1} . The difference between these rates implies that at least part of the contrail deepening was the result of lofting by vertical motions within the contrail. In contrast, the fall speed derived for contrails from stereography and flight track data suggests that contrail fall speeds may have been slightly larger ($0.12\text{--}0.16 \text{ m s}^{-1}$).

The two remote sensing analyses gave divergent results of some cloud properties. Optical depths from the VISST are typically about twice as large as those retrieved from the FCT method. For a nebulous cloud like contrails or cirrus, the VISST-retrieved value of T_c should correspond to some altitude between the cloud top and bottom. Thus, the retrieved temperatures should be at some level below the cloud top. For spreading contrails, the difference between cloud top and the effective radiating altitude should be less than 1 km. The stereographic results and the minimum level of saturated air in the soundings suggests that the mean VISST cloud heights are far too low and optical depths are too large while τ_c from the FCT method is more accurate. The FCT approach, however, does not provide any information on the vertical distribution and evolution of the contrails. Optical depths corresponding to the maximum

heights are probably the most accurate values because they are closest to and follow the trends in the stereographically determined cloud-top heights; but they do not represent the entire cloud field. Although the mean VISST-derived optical depths are too large, the relative trends in height and optical depth are reasonable. Furthermore, the longwave radiative forcing computed using the VISST-retrieved cloud properties should be comparable to that from the FCT approach because the greater cloud temperatures would offset the greater optical depths.

The large differences between the VISST and the FCT optical depths and between the VISST and stereographic heights are likely the result of several factors. As noted earlier, the thinness of the contrails makes retrievals of contrail optical depth more difficult for visible channel-based retrievals. As the actual optical depth decreases, the retrieved value becomes increasingly sensitive to errors in the clear-sky radiances. The VISST pixel-level retrievals use estimates of clear-sky radiances corresponding to an average for a generally much larger area ($> 1024 \text{ km}^2$). The variabilities in the clear-sky reflectances and temperatures are not taken into account so that, on average, τ_v for optically thin clouds ($\tau_v < 0.4$) is often overestimated. No solutions are possible for the darker pixels (thin cloud over the dark portion) and the brighter pixels (those over the brighter portion of the background) yield larger than actual optical depths. The average result for a given scene is an overestimate of τ_v . This notion is reinforced with the use of the Layer Bispectral Threshold Method (LBTM; Minnis et al. 1995a) applied to the same data. The LBTM includes the darker pixels through averaging, hence reducing the mean optical depth and raising the cloud heights. For example, selected retrievals using both the LBTM and the VISST for contrails over Lakes Michigan and Superior at 1945 UTC yield average optical depths of 0.31 and 0.37, respectively, and average heights of 7.9 and 6.2 km, respectively. The mean LBTM heights are still 1.3 km below the maximum VISST values which most likely

correspond to pixels with backgrounds most closely matching the prescribed values. Thus, the dark pixel problem can only account for a portion of the underestimation in τ .

Another factor that may help to explain the optical depth discrepancies is the difference in scattering between the modeled ice crystal shape and the actual shape of the contrail ice crystals. Since the contrails are optically thin, most of the reflected light observed by the satellites would be singly-scattering light, making phase function differences important to the retrieval of cloud properties. Both the VISST and LBTM retrievals are based on a hexagonal column model (Minnis et al., 1998), while many of the particles in the core of a contrail (especially a young contrail) are probably spherical or quasi-spherical in shape (Schröder et al., 2000). Calculations of ice crystal scattering at visible wavelengths (Liou et al., 2000) show that hexagonal ice columns have much larger scattering at 180° and between 70° – 120° than ice spheres, while they have less scattering than spheres at angles around 125° – 140° . As mentioned earlier, the scattering angle of the *GOES-8* observations at 1645 UTC over the upper peninsula of Michigan was approximately 179° . If the contrails were mostly composed of nearly spherical particles, the actual reflectance of the contrails at 1645 UTC would be significantly less than that expected from the VISST algorithm, leading to an underestimate of cloud optical depth (and probably an overestimate of cloud particle size since that quantity is based largely on the solar infrared reflectance). Similar underestimates of τ would occur between 2045 and 2145 UTC, when the observed scattering angle was between 119° and 104° . The largest contrail optical depths are retrieved between 1915 and 2015 UTC, when the scattering angle observed from the satellite is 142° and 127° , respectively. If the visible light scattering at these angles is much larger for contrail particles than hexagonal columns (as suggested by Fig. 3 in Liou et al. (2000)), the retrieved optical depths will be larger than the actual values. This hypothesis suggests,

however, that most of the contrail particles would have to remain quasi-spherical over the lifetime of the clouds, an unlikely occurrence in growing contrails.

Comparisons of model calculations of infrared temperatures and reflectances for different phase functions with the variation of observed values from GOES-8 at 1645 UTC yield mixed results. A water droplet model fits the data better in a few cases while a hexagonal model is more reasonable in others. Similar comparisons at 1945 UTC indicate that the small crystal ice model yields smaller τ and greater heights in all cases.

The VISST retrievals from *Terra* MODIS overpasses at 1623 and 1801 UTC (see Fig. 7) suggest that the phase function does not contribute significantly to the optical depth underestimate. The scattering angle for the *GOES-8 (Terra)* at 1623 UTC is 173° (131°), while at 1801 UTC the angle is 160° (97°), yet the MODIS optical depths are within 10% of the GOES-8 values, not enough to account for the height differences. However, the *Terra* results themselves are consistent with the particle-shape hypothesis since an underestimate of optical depth would be expected at 1801 UTC compared to 1623 UTC. Although it could be argued that the agreement between the *GOES-8* and *Terra* optical depth retrievals is the result a compensating error due to a difference in calibration between the satellites, the differences in cloud particle size retrievals between 1623 UTC and 1801 UTC cannot be explained by either particle shape or calibration differences alone.

Finally, other sources of error in the retrievals include the errors in the parameterization and the possibility that some scattered midlevel clouds developed in some areas underneath the cirrus and affected the retrievals. Midlevel clouds were prevalent east of the study area and could be seen in the $3.9\text{-}\mu\text{m}$ imagery over some parts of the study region. The soundings also suggest the potential for the development of scattered altocumulus clouds between 4 and 6 km.

The few surface observations available did not record any midlevel cloud cover, however. The VISST parameterization should reproduce the visible-channel reflectances to within $\pm 2\%$ compared to adding-doubling radiative transfer calculations for very thin clouds. However, errors in the specified Rayleigh scattering, ozone loading, the occurrence of significant aerosol concentrations, and error in calculating the surface reflectance could result in some biased reflectances leading to errors in τ . An infrared approach would avoid many of these problems associated with the optically thin clouds.

Figure 8 demonstrates that the air traffic density in the region where contrails formed was relatively uniform. The mean air traffic density per $1^\circ \times 1^\circ$ grid cell for flights with altitudes greater than or equal to 30,000 ft was usually only 4 per hour in the region where contrails formed, which may account for the overall uniformity and clarity of the identified contrail segments. As suggested by the non-linear shape of the air traffic/contrail density relationship in Fig. 11, observed contrail densities probably reach an asymptotic limit in the GOES imagery at higher air traffic densities. This limit would be due to both the smearing of multiple contrails in satellite imagery and the production of fewer contrails growing wide enough to be seen in the imagery because of competition for water vapor. The formation of the cirrus deck seen in Fig. 1 is an example of smearing of the individual contrails in areas with dense air traffic. The matching of contrail density data with air traffic data showed that approximately 10 percent of the flights produced contrails wide enough to be seen in *GOES-8* imagery.

6. CONCLUSIONS

This study has provided the first detailed analysis of contrail formation and motion using actual flight data integrated into numerical weather analyses. The contrail outbreak analyzed here

reveals a clear case of relative humidities that exceed ice saturation at flight level over an area where no natural cirrus were forming over the course of the day. These results also reinforce the need for adjustment of the RHI fields from rawinsondes and numerical weather prediction models, even in high-resolution models such as the RUC, which also have sophisticated cloud/moisture parameterizations. Grid-averaging effects and the difficulty in measuring upper tropospheric moisture lead to a dry bias in model analyses. More studies are necessary to conclusively determine the magnitude of this adjustment. Applying an RHI adjustment, however, should bring theory and observations into closer agreement.

The analysis results also highlight the difficulties in retrieving microphysical properties of optically thin ice clouds using reflected solar radiation. Use of radiances at other wavelengths such as 1.38, 3.9, 8.5, and 12 μm may yield more accurate objective results. The stereographic analyses verified to first order that the contrail height can be assumed to be constant throughout its lifetime and, therefore, the contrail temperature can be specified to effect a simple infrared retrieval like that used by Meyer et al. (2002). The underestimated VISST optical depths suggest that the optical depth value of 0.3, considered as the best estimate in the study by Minnis et al. (1999) to compute global contrail radiative forcing, is probably too large. Based on the results of Meyer et al. (2002) and the current results, the average value is more likely to be between 0.10 and 0.20.

Contrail formation density was roughly correlated with air traffic density after the effects of competing cloud coverage, humidity and vertical velocity were considered. The RUC vertical velocity analyses showed that vertical velocity has an important effect on contrail formation, as regions with negative vertical velocities over 0.015 m s^{-1} in magnitude produced no contrails even when the RHI was above the 85% threshold.

A surprising result from this study is that the linear contrail detection algorithm developed by Mannstein et al. (1999) for application to 1-km infrared satellite imagery produced nearly identical amounts of contrail coverage using 4-km GOES-8 (actually 6 km for the given viewing angle) and 1-km AVHRR data. The single case study, however, is insufficient to conclude that comparable results will always be obtained. Many more comparisons are needed to reach any firm conclusion. The results also confirmed earlier studies that the linear-contrail coverage approach underestimates the contrail-induced cirrus coverage. Although contrail spreading has been examined in several previous studies, there have been no direct comparisons between the automated retrievals and the more subjective contrail cirrus coverage determined subjectively from satellite loops. The factor-of=2 difference found here for the aged contrail cirrus versus the automated linear contrail coverage is smaller than estimated in the previous studies but is still a significant factor.

The analysis procedures developed here provide the framework for realistic simulations of contrail lifecycles and interactions. Despite the difficulties in determining upper tropospheric humidity, the locations of the contrails in this example confirm that the growth and longevity of contrails is explained by the general Appleman temperature/relative humidity criteria. The frequency of atmospheric conditions favorable for the development of widespread persistent contrails could be estimated by examining numerical weather model analyses like the RUC if the fields are adjusted for RHI and the dry bias. Much additional research is required, however, to parameterize contrail spreading, precipitation, and dissipation. Although it is currently possible to simulate contrails and cirrus to some degree, it will be difficult to realistically simulate contrails and cirrus clouds using the current relative humidity datasets without adjustments because the mechanisms for naturally producing cirrus clouds require values of RHI that do not

appear in current operational measuring systems. Without the proper humidities, the physics of the formation process must be altered to produce cirrus in detailed models. Improved measurements of moisture in the upper troposphere, therefore, remain a critical need for accurate modeling of upper level clouds and contrails.

Acknowledgements. This research was supported by grants NASA NAG-1-2135 and NAG-1-02044 and by the NASA Pathfinder Program. The authors wish to thank Sunny Sun-Mack and Kirk Ayers for the VISST retrievals, and Donald Garber for his help on the stereographic analyses.

REFERENCES

- Appleman, H., 1953: The formation of exhaust condensation trails by jet aircraft. *Bull. Amer. Meteor. Soc.*, **34**, 14-20.
- Arduini, R. F., P. Minnis, and D. F. Young, 2002: Investigation of a visible reflectance parameterization for determining cloud properties in multi-layered clouds. *Proc. AMS 11th Conf. Cloud Physics*, Ogden, UT, June 3-7.
- Benjamin, S. G., J. M. Brown, K. J. Brundage, B. E. Schwartz, T. G. Smirnova, and T. L. Smith, 1998: The operational RUC-2. *Proc. AMS 16th Conf. Weather Analysis and Forecasting*, Phoenix, AZ, 249-252.
- Busen, R., and U. Schumann, 1995: Visible contrail formation from fuels with different sulfur contents. *Geophys. Res. Lett.*, **22**, 1357-1360.
- Dong, X., P. Minnis, G. G. Mace, W. L. Smith, Jr., M. Poellot, R. T. Marchand, and A. D. Rapp, 2002: Comparison of stratus cloud properties deduced from surface, GOES, and aircraft data during the March 2000 ARM Cloud IOP. *J. Atmos. Sci.*, **59**, 3256-3284.
- Duda, D. P., P. Minnis, and L. Nguyen, 2001: Estimates of cloud radiative forcing in contrail clusters using GOES imagery. *J. Geophys. Res.*, **106** (D5), 4927-4937.
- , P. Minnis, W. L. Smith, Jr., S. Sun-Mack, J. K. Ayers, J.-F. Gayet, F. Auriol, J. Ström, A. Minikin, A. Petzold, and U. Schumann, 2002: An interhemispheric comparison of cirrus cloud properties using MODIS and GOES. *Proc. 11th AMS Conf. Atmos. Radiation*, Ogden, UT, June 3-7, J17-J20.
- Elliott, W. P., and D. J. Gaffen, 1991: On the utility of radiosonde humidity archives for climate studies. *Bull. Amer. Meteor. Soc.*, **72**, 1507-1520.

- Fujita, T. T., 1982: Principle of stereographic height computations and their applications to stratospheric cirrus over severe thunderstorms. *J. Meteorol. Soc. Japan*, **60**, 355-368.
- Heymsfield, A. J., and J. Iaquinta, 1999: Cirrus crystal terminal velocities. *J. Atmos. Sci.*, **57**, 916-938.
- Jensen, E. J., A. S. Ackerman, D. E. Stevens, O. B. Toon, and P. Minnis, 1998: Spreading and growth of contrails in a sheared environment. *J. Geophys. Res.*, **103**, 31,557-31,567.
- Liou, K. N., Y. Takano, and P. Yang, 2000: Light scattering and radiative transfer in ice crystal clouds: Applications to climate research. *Light scattering by nonspherical particles: Theory, measurements, and applications*, M. I. Mishchenko, J. W. Hovenier, L. D. Travis, Eds., Academic Press, 417-449.
- Mace, G. G., T. P. Ackerman, P. Minnis, and D. F. Young, 1998: Cirrus layer microphysical properties derived from surface-based millimeter radar and infrared interferometer data. *J. Geophys. Res.*, **103** (D18), 23,207-23,216.
- Mannstein, H., R. Meyer, and P. Wendling, 1999: Operational detection of contrails from NOAA-AVHRR data. *Intl. J. Remote Sens.*, **20**, 1641-1660.
- Meyer, R., H. Mannstein, R. Meerkotter, U. Schumann and P. Wendling, 2002: Regional radiative forcing by line-shaped contrails derived from satellite data. In press *J. Geophys. Res.*, **107** (D10), doi: 10.1029/2001JD000426, 15 pp., 31 May 2002.
- Miloshevich, L. M., H. Vömel, A. Paukkunen, A. J. Heymsfield, and S. J. Oltmans, 2001: Characterization and correction of relative humidity measurements from Vaisala RS80-A radiosondes at cold temperatures, *J. Atmos. Oceanic Technol.*, **18**, 135-156.

- Minnis, P., D. F. Young, K. Sassen, J. M. Alvarez, and C. J. Grund, 1990: The 27-28 October 1986 FIRE IFO Case Study: Cirrus parameter relationships derived from satellite and lidar data. *Mon. Wea. Rev.*, **118**, 2402 - 2425.
- , D. F. Young, and E. F. Harrison, 1991: Examination of the relationship between outgoing infrared window and total longwave fluxes using satellite data, *J. Climate*, **4**, 1114-1133.
- , P. W. Heck, and D. F. Young, 1993: Inference of cirrus cloud properties using satellite-observed visible and infrared radiances, Part II: Verification of theoretical cirrus radiative properties. *J. Atmos. Sci.*, **50**, 1305-1322.
- , and Coauthors, 1995a: Cloud optical property retrieval (subsystem 4.3). Cloud analyses and radiance inversions (subsystem 4), Vol. III, Clouds and the Earth's Radiant Energy System (CERES) algorithm theoretical basis document, NASA Ref. Publ. 1376, Vol. 3, 135-176. Available at <http://techreports.larc.nasa.gov/ltrs/95/NASA-95-rp1376vol3.refer.html>.
- , W. L. Smith, Jr., D. P. Garber, J. K. Ayers, and D. R. Doelling, 1995b: Cloud Properties Derived From GOES-7 for the Spring 1994 ARM Intensive Observing Period Using Version 1.0.0 of the ARM Satellite Data Analysis Program. *NASA RP 1366*, 59 pp. Available at <http://techreports.larc.nasa.gov/ltrs/95/NASA-95-rp1366.refer.html>.
- , D. P. Garber, D. F. Young, R. F. Arduini, and Y. Takano, 1998: Parameterization of reflectance and effective emittance for satellite remote sensing of cloud properties. *J. Atmos. Sci.*, **55**, 3313-3339.
- , U. Schumann, D. R. Doelling, K. M. Gierens, and D. W. Fahey, 1999: Global distribution of contrail radiative forcing. *Geophys. Res. Lett.*, **26**, 1853-1856.

- , L. Nguyen, D. P. Duda, and R. Palikonda, 2002a: Spreading of isolated contrails during the 2001 air traffic shutdown. *Proc. AMS 10th Conf. Aviation, Range, and Aerospace Meteor.*, Portland, OR, May 13-16.
- , D. F. Young, B. A. Weilicki, S. Sun-Mack, Q. Z. Trepte, Y. Chen, P. W. Heck, and X. Dong, 2002b: A global cloud database from VIRS and MODIS for CERES. *Proc. SPIE 3rd Intl. Asia-Pacific Environ. Remote Sensing Symp. 2002: Remote Sens. of Atmosphere, Ocean, Environment, and Space*, Hangzhou, China, October 23-27. Available at <http://www-pm.larc.nasa.gov/ceres/pub/conference/Minnis.SPIE.02.pdf>
- Ponater, M., S. Marquart, and R. Sausen, 2002: Contrails in a comprehensive global climate model: Parameterization and radiative forcing results. *J. Geophys. Res.*, **107** (D15), doi: 10.1029/2001JD000429, 03 July 2002.
- Pruppacher, H. R., and J. D. Klett, 1980: *Microphysics of Clouds and Precipitation*. D. Reidel, pp.714.
- Sassen, K., 1997: Contrail cirrus and their potential for regional climate change. *Bull. Amer. Meteor. Soc.*, **78**, 1885-1903.
- , and G. C. Dodd, 1989: Haze particle nucleation simulations in cirrus clouds, and applications for numerical and lidar studies. *J. Atmos. Sci.*, **46**, 3005-3014.
- Sausen, R., K. Gierens, M. Ponater, and U. Schumann, 1998: A diagnostic study of the global coverage by contrails. Part I: Present day climate. *Theor. Appl. Clim.*, **61**, 127-141.
- Schrader, M. L., 1997: Calculations of aircraft contrail formation critical temperatures. *J. Appl. Meteor.*, **36**, 1725-1729.

- Schröder, F., B. Kärcher, C. Durore, J. Strom, A. Petzold, J.-F., Gayet, B. Strauss, P. Wendling, and S. Borrmann, 2000: On the transition of contrails into cirrus clouds. *J. Atmos. Sci.*, **57**, 464-480.
- Young, D. F., P. Minnis, D. Baumgardner, and H. Gerber, 1998: Comparison of in situ and satellite-derived cloud properties during SUCCESS. *Geophys. Res. Lett.*, **25**, 1125-1128.

Table Captions

Table 1. Flights from the FT database with the lowest mean D_s value throughout the analysis period from 11 selected contrails. The contrail fall speed was 0.00 m s^{-1} relative to the RUC vertical wind field.

Table 1. Flights from the FT database with the lowest mean D_s value throughout the analysis period from 11 selected contrails. The contrail fall speed was 0.00 m s^{-1} relative to the RUC vertical wind field.

Flight Name	Original Altitude of Flight [mean] (ft)	Time needed for <i>GOES-8</i> visibility (hr)	Mean D_s (km)	D_s of other nearest flights
ACA113	35,000	1.417	16.94	CDN628: 28.66
ACA163	39,000	1.050	5.36	CDN911: 13.02
ACA177	39,000	1.417	5.00	KAL251: 17.74
				ROY818: 9.47
				CDN955: 9.63
				ACA185: 15.11
ANA010	37,000	0.600	12.75	KAL081: 57.62
KAL081	37,000	0.667	12.74	ANA010: 49.32
NWA18	37,000	0.900	10.52	
AAL55	35,000	1.017	13.95	AAL37: 66.88
CPA082	37,000	1.150	4.71	CMM344: 26.09
CDN902	37,000	1.167	8.38	CDN574: 43.60
CDN574	37,000	1.167	12.12	CDN902: 55.03
KAL252	35,000	1.083	6.56	CDN574: 37.02

Figure Captions

Fig. 1. *NOAA-14* AVHRR infrared image of persistent contrails over the western Great Lakes, 2050 UTC, 9 October 2000.

Fig. 2. Enhanced *GOES-8* image at 1945 UTC 9 October 2000. The gray rectangular boxes are the areas analyzed with both the Mannstein et al. (1999) contrail detection algorithm and a subjective manual inspection. The box marked by thick white lines is the portion of the contrail-generated cirrus analyzed with LBTM and VISST.

Fig. 3. Linear contrail coverage (km^2) determined from Mannstein et al. (1999) objective technique on *GOES-8* imagery (solid line) and AVHRR imagery (solid circle) and contrail coverage determined from a subjective manual inspection of *GOES-8* imagery (dotted line). The manual inspection includes linear contrails and more diffuse cirrus clouds judged to be formed from earlier linear contrails.

Fig. 4. Contrail spreading based on RUC wind analyses assuming several contrail fall speed/vertical deepening rates and from *GOES-8* observations.

Fig. 5. (a) Several time series of retrieved contrail optical depth using the FCT and VISST remote sensing methods and two satellites. (b) Unit contrail longwave radiative forcing (in W m^{-2}) for Loop A (solid line) and Loop B (dotted line).

Fig. 6. (a) Rawinsonde temperatures and dew point temperatures measured at Gaylord MI (APX) and Green Bay WI (GRB) at 00 UTC 10 October 2000 as a function of height. (b) The relative humidity with respect to ice (RHI) measured at APX and GRB at 00 UTC 10 October 2000. For heights with temperatures below 243 K, the RHI values have been adjusted following Minnis et al. (2002a).

Fig. 7. (a) Time series of VISST-retrieved effective ice crystal sizes from *GOES-8* (lines and circles) and mean effective ice crystal sizes from *Terra* MODIS observations (crosses) on 9 October 2000. (b) Same as (a), but for VISST-retrieved visible optical depth. (c) VISST-retrieved mean (solid line) and median (dotted line) effective cloud height from *GOES-8* and mean effective cloud heights (crosses) from *Terra* MODIS observations on 9 October 2000. The maximum VISST cloud heights retrieved from *GOES-8* are shown as solid triangles, while the plus signs represent the maximum VISST cloud heights retrieved from *Terra* MODIS. The open circles with the error bars are the mean and range of the cloud heights estimated from stereography measurements.

Fig. 8. Contrails visually identified in *GOES-8* imagery (thick lines) at 1745 UTC 9 October 2000, and all flight tracks from FlyteTrax between 1000 and 1745 UTC that occur in areas where the interpolated RUC model RHI at 225 hPa is greater than or equal to 85% (thin lines).

Fig. 9. Contrails visually identified in *GOES-8* imagery (thick lines) matched with the nearest flight tracks of commercial aircraft from FlyteTrax (thin lines) at 1745 UTC 9 October 2000. Flight tracks from earlier times were advected to the present time using the RUC horizontal winds at the level corresponding to the flight track altitude.

Fig. 10. Mean distance error (D_s) of the 11 selected flight tracks in Table 1 as a function of the contrail fall speed. The squares represent the mean error of the flight tracks.

Fig. 11. Contrail density (per $1^\circ \times 1^\circ$ deg grid box per hour) versus air traffic density (per $1^\circ \times 1^\circ$ deg grid box per hour) for a twelve-hour period over Great Lakes region on 9 October 2000.

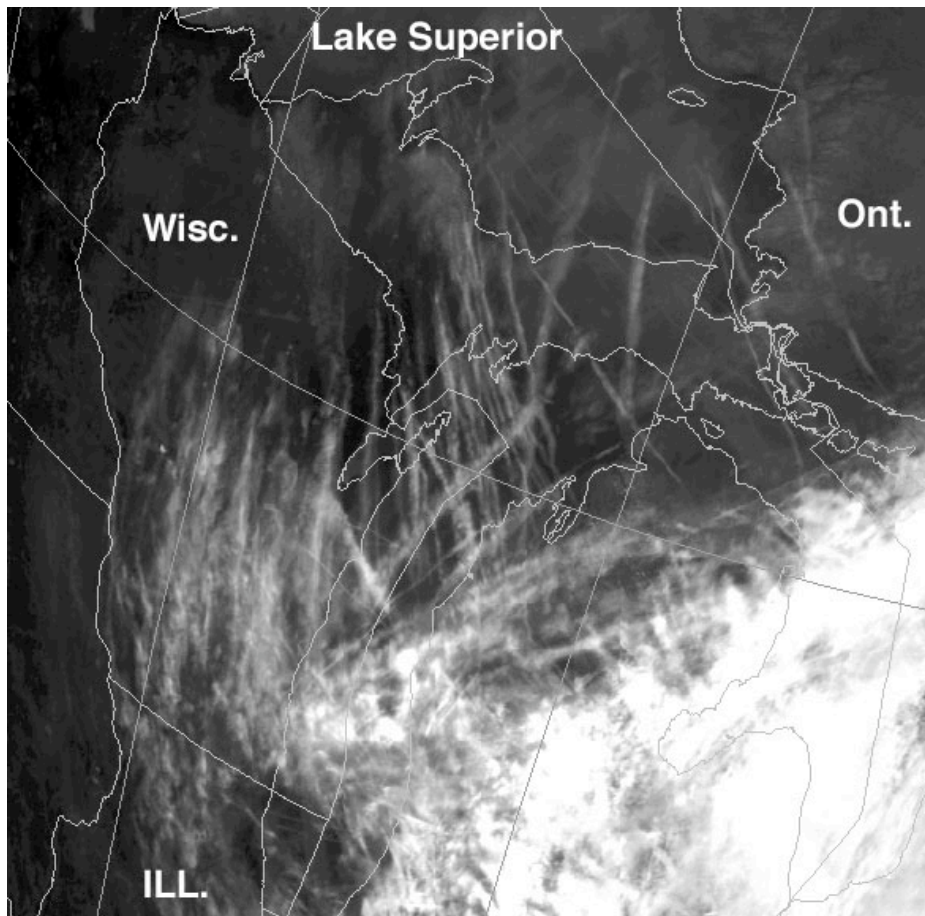


Figure 1. *NOAA-14* AVHRR infrared image of persistent contrails over the western Great Lakes, 2050 UTC, 9 October 2000.

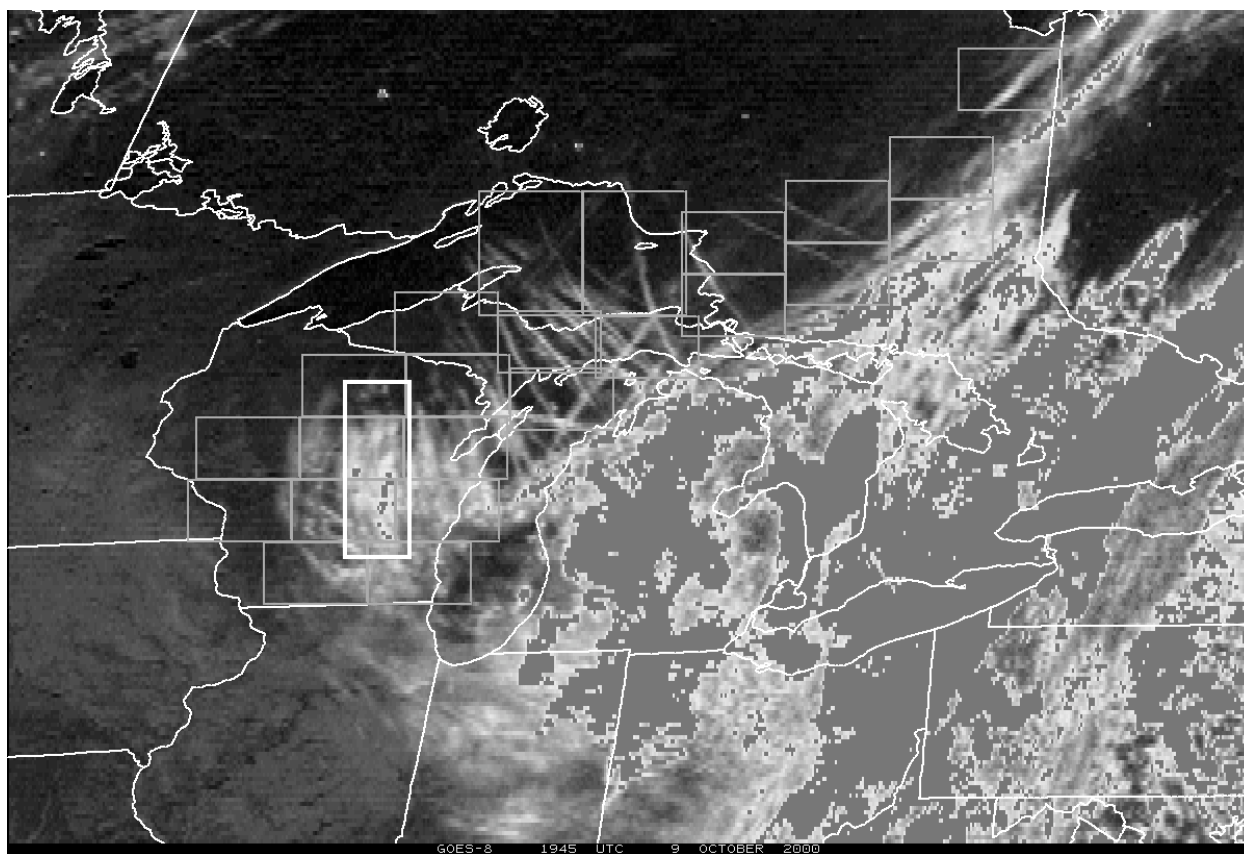


Figure 2. Enhanced *GOES-8* image at 1945 UTC 9 October 2000. The gray rectangular boxes are the areas analyzed with both the Mannstein et al. (1999) contrail detection algorithm and a subjective manual inspection. The box marked by thick white lines is the portion of the contrail-generated cirrus analyzed with LBTM and VISST.

Contrail Areal Coverage

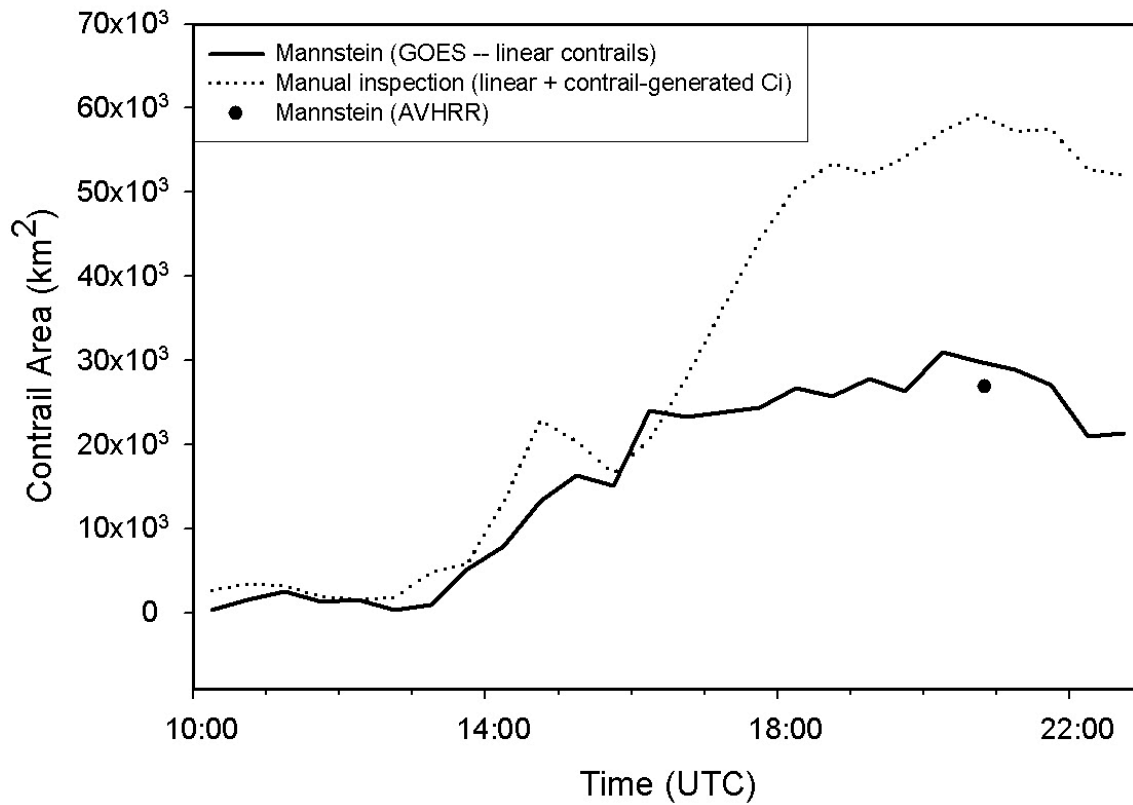


Figure 3. Linear contrail coverage (km^2) determined from Mannstein et al. (1999) objective technique on *GOES-8* imagery (solid line) and AVHRR imagery (solid circle) and contrail coverage determined from a subjective manual inspection of *GOES-8* imagery (dotted line). The manual inspection includes linear contrails and more diffuse cirrus clouds judged to be formed from earlier linear contrails.

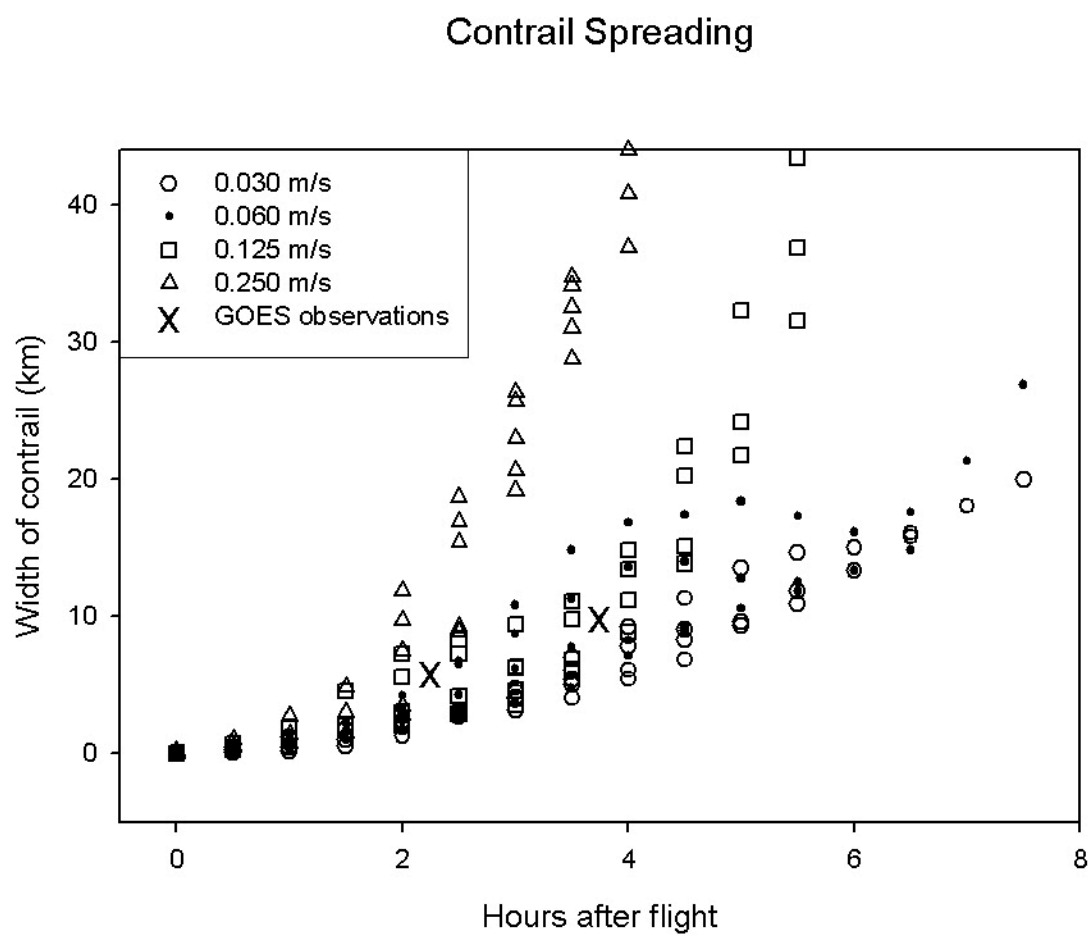


Figure 4. Contrail spreading based on RUC wind analyses assuming several contrail fall speed/vertical deepening rates and from *GOES-8* observations.

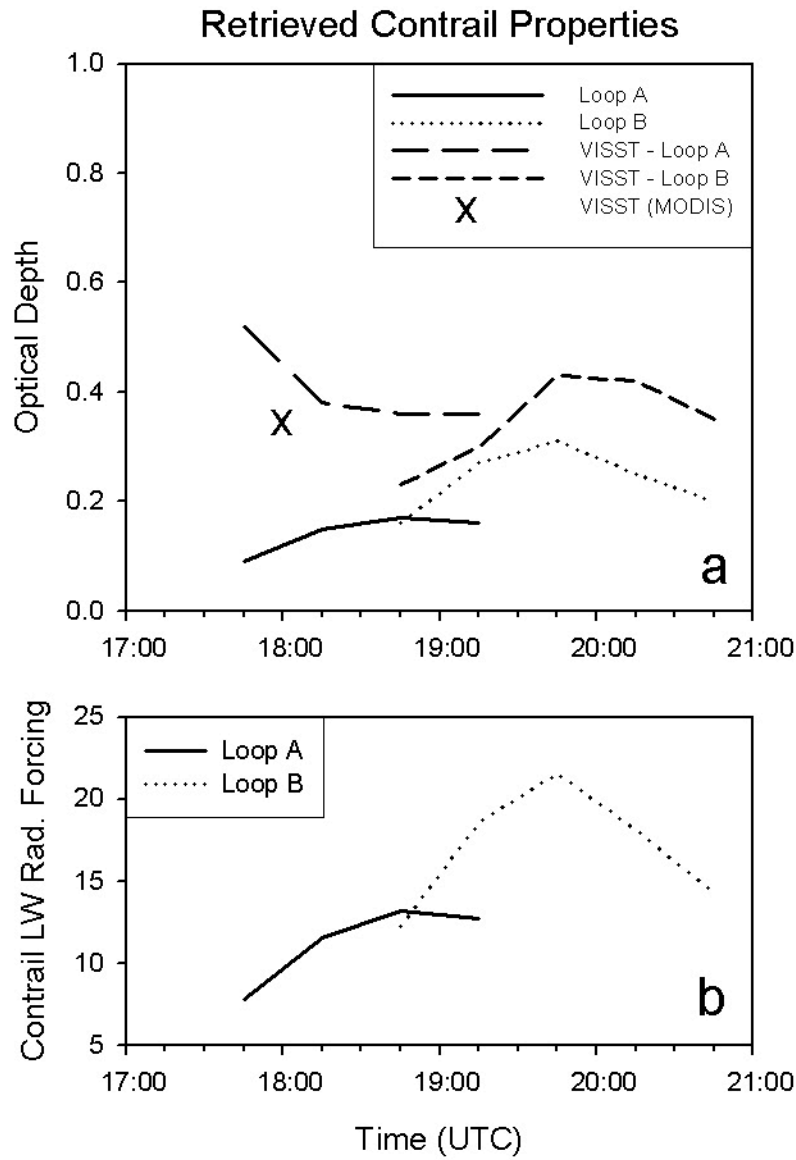


Figure 5. (a) Several time series of retrieved contrail optical depth using the FCT and VISST remote sensing methods and two satellites. (b) Unit contrail longwave radiative forcing (in W m^{-2}) for Loop A (solid line) and Loop B (dotted line).

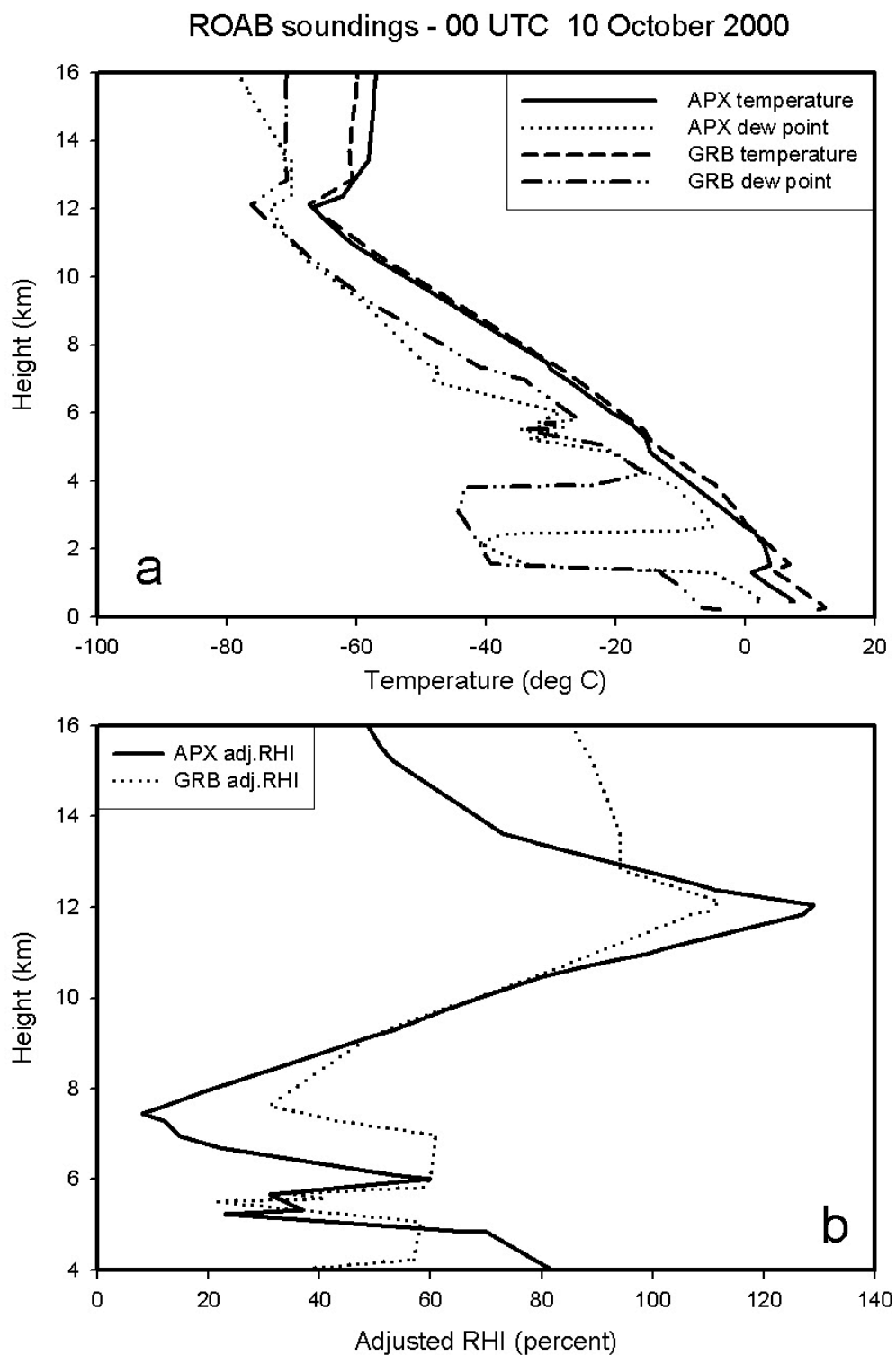


Figure 6. (a) Rawinsonde temperatures and dew point temperatures measured at Gaylord MI (APX) and Green Bay WI (GRB) at 00 UTC 10 October 2000 as a function of height. (b) The relative humidity with respect to ice (RHI) measured at APX and GRB at 00 UTC 10 October 2000. For heights with temperatures below 243 K, the RHI values have been adjusted following Minnis et al. (2002a).

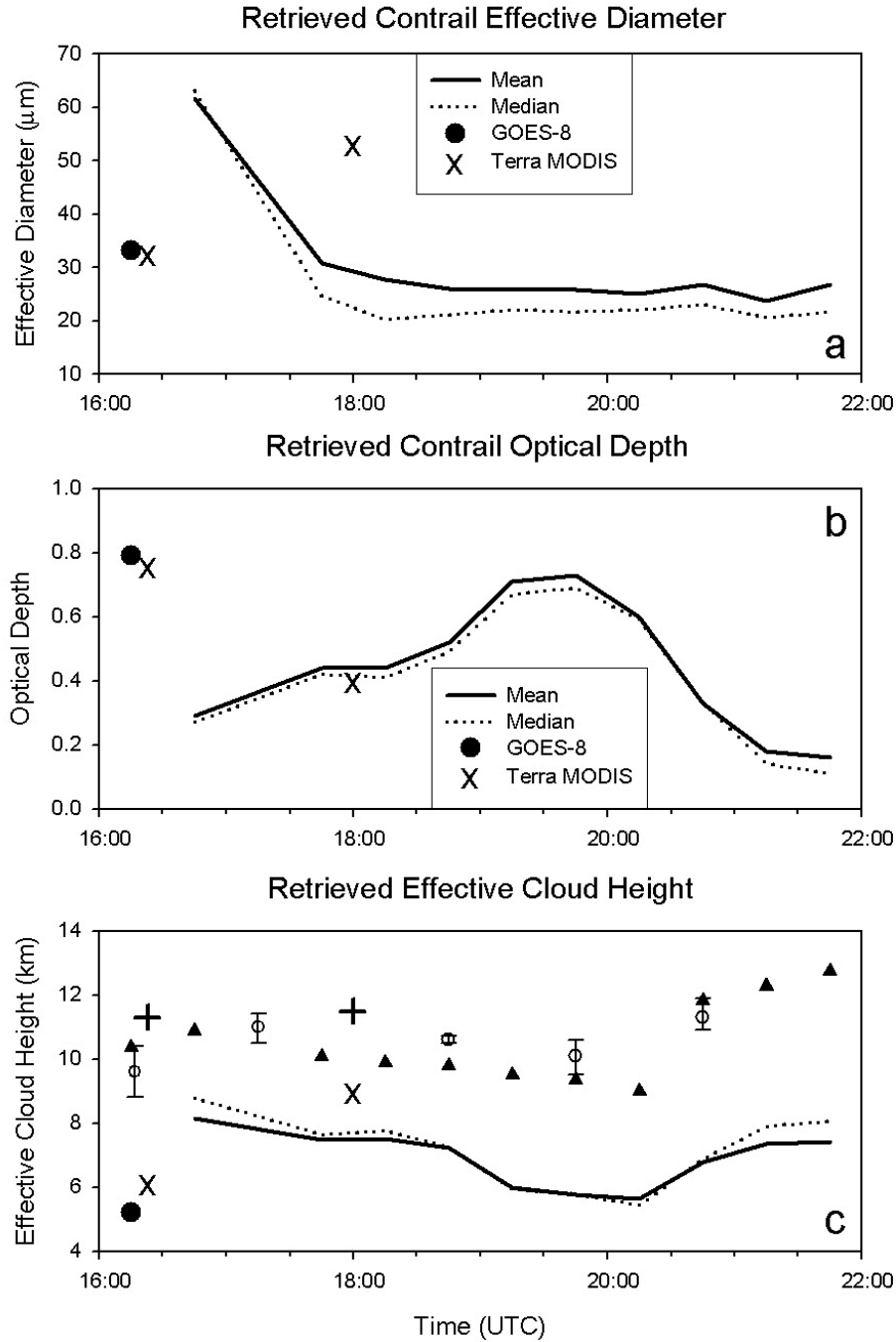


Figure 7. (a) Time series of VISST-retrieved effective ice crystal sizes from *GOES-8* (lines and circles) and mean effective ice crystal sizes from *Terra* MODIS observations (crosses) on 9 October 2000. (b) Same as (a), but for VISST-retrieved visible optical depth. (c) VISST-retrieved mean (solid line) and median (dotted line) effective cloud height from *GOES-8* and mean effective cloud heights (crosses) from *Terra* MODIS observations on 9 October 2000. The maximum VISST cloud heights retrieved from *GOES-8* are shown as solid triangles, while the plus signs represent the maximum VISST cloud heights retrieved from *Terra* MODIS. The open circles with the error bars are the mean and range of the cloud heights estimated from stereography measurements.

17:45 UTC 9 October 2000

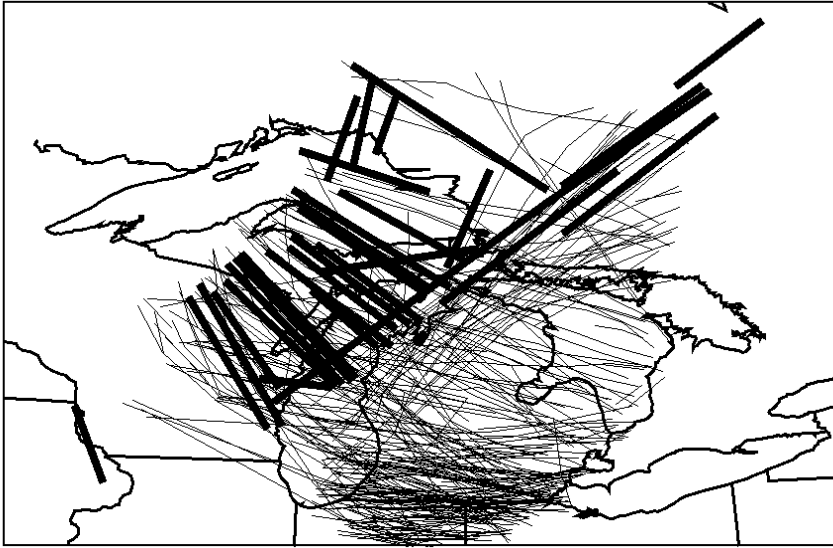


Figure 8. Contrails visually identified in *GOES-8* imagery (thick lines) at 1745 UTC 9 October 2000, and all flight tracks from FlyteTrax between 1000 and 1745 UTC that occur in areas where the interpolated RUC model RHI at 225 hPa is greater than or equal to 85% (thin lines).

17:45 UTC 9 October 2000

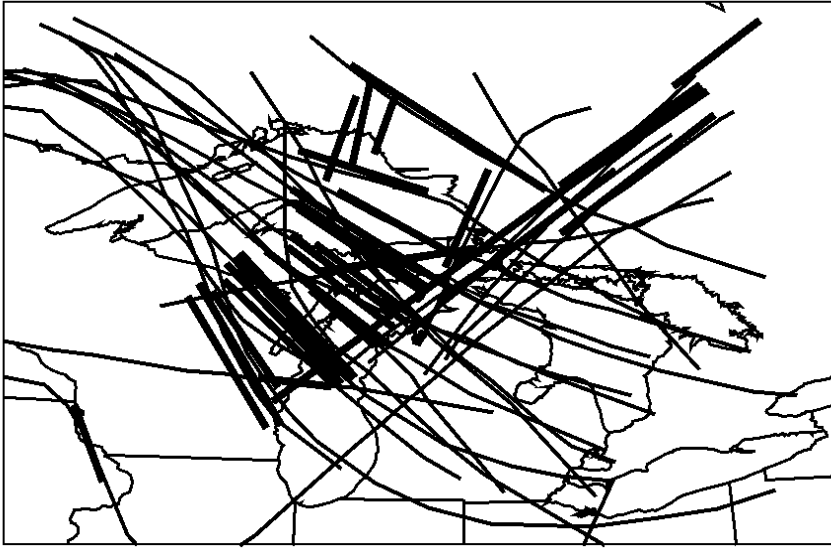


Figure 9. Contrails visually identified in *GOES-8* imagery (thick lines) matched with the nearest flight tracks of commercial aircraft from FlyteTrax (thin lines) at 1745 UTC 9 October 2000. Flight tracks from earlier times were advected to the present time using the RUC horizontal winds at the level corresponding to the flight track altitude.

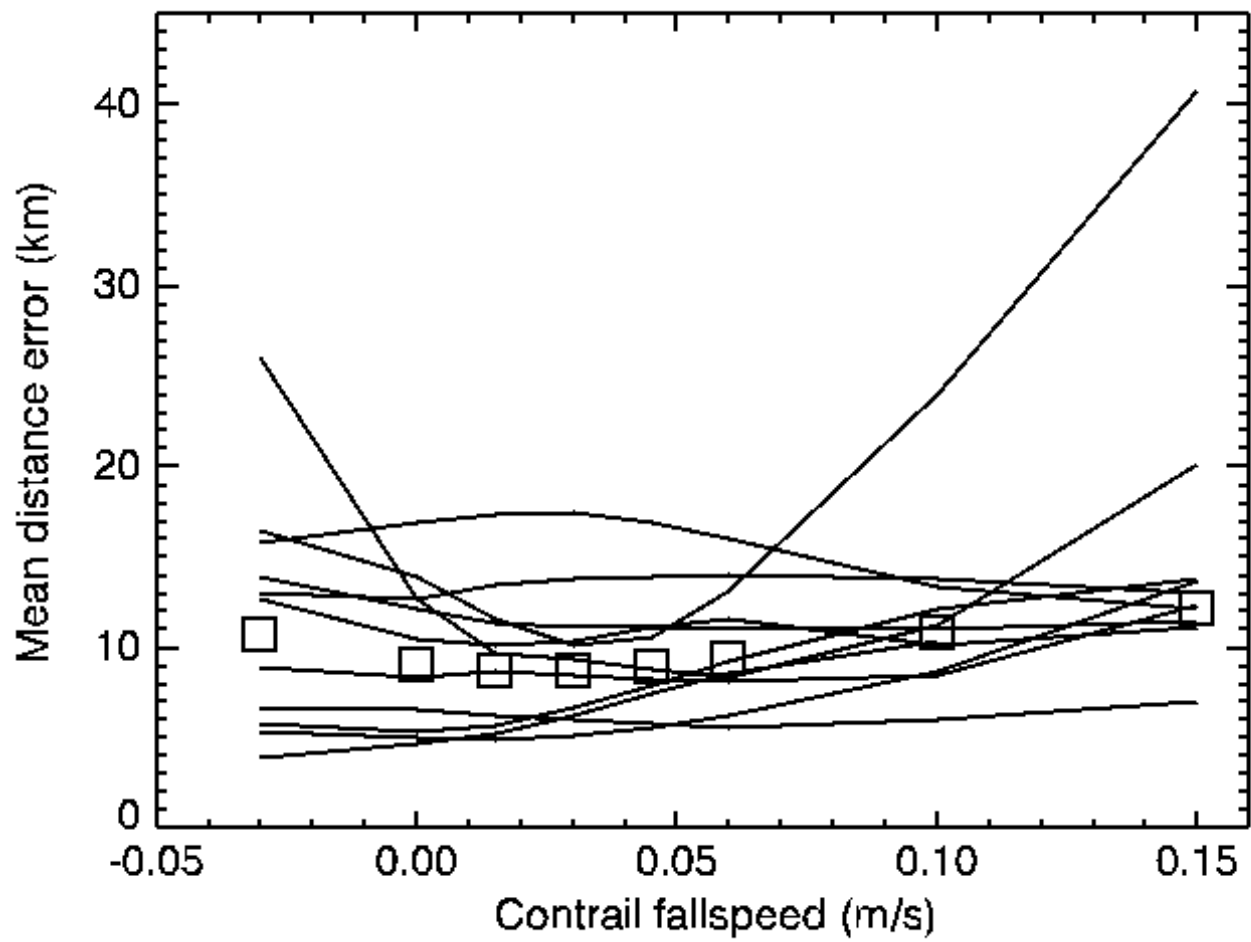


Figure 10. Mean distance error (D_s) of the 11 selected flight tracks in Table 1 as a function of the contrail fall speed. The squares represent the mean error of the flight tracks.

